An Overview of Ultra-Wideband Microwave Imaging via Space-Time Beamforming for Early-Stage Breast-Cancer Detection

Xu Li[1], Essex J. Bond[2], Barry D. Van Veen[2], and Susan C. Hagness[2]

[1]Department of Biomedical Engineering, Northwestern University
2145 Sheridan Road, Evanston, IL 60208 USA
E-mail: xuli@northwestern.edu

[2]Department of Electrical and Computer Engineering, University of Wisconsin
1415 Engineering Drive, Madison, WI 53706 USA
E-mail: ejbond@wisc.edu, vanveen@engr.wisc.edu, hagness@engr.wisc.edu

Abstract

Ultra-wideband (UWB) microwave imaging has recently been proposed for detecting small malignant breast tumors. In this article, we review the current research status of this approach. First, we introduce the concept of microwave imaging via space-time (MIST) beamforming and related signal-processing algorithms. The objective of these signal-processing techniques is to form a spatial image of scattered microwave energy, and to identify the presence and location of malignant lesions from their scattering signatures. Next, we present numerical studies based on Finite-Difference Time-Domain simulations to demonstrate the efficacy of MIST beamforming for detecting small malignant breast lesions in both prone and supine configurations. Finally, the experimental feasibility of UWB microwave imaging is demonstrated using an initial imaging prototype and multilayered breast phantoms.

Keywords: Biomedical electromagnetic imaging; breast cancer; microwave imaging; ultra-wideband radar; array signal processing; FDTD methods; microwave measurements

1. Introduction

Ultra-wideband (UWB) radar techniques are used in many subsurface sensing applications, such as detecting unexploded land mines, locating utility lines, examining archaeology sites, and studying groundwater [1]. UWB radar systems usually do not attempt to reconstruct the complete profile of the dielectric properties of the region of interest, but instead seek to identify the presence and location of "targets" by their scattering signatures. In a basic UWB radar configuration, a transmitting antenna radiates extremely short duration (on the order of tens of picoseconds to nanoseconds) bursts of RF/microwave energy. The transmitted electromagnetic (EM) waves penetrate into the region under inspection, and are scattered by any targets that exhibit a mismatch in dielectric properties. These scattered signals are recorded by one or more receiving antennas, and then used to infer the existence, location, and characteristics of the subsurface targets.

Recently, a medical application of UWB radar techniques has been proposed by Hagness et al., where miniature versions of UWB microwave radars are used for detecting malignant tumors in the breast [2, 3]. Several groups around the world – in addition to the University of Wisconsin-Madison – are now engaged in research related to this proposed UWB microwave radar application [4-14]. These ongoing investigations are motivated by the critical need for developing early-stage breast-cancer screening tools with high sensitivity and specificity.

In this article, we review the status of microwave imaging via space-time (MIST) beamforming, a representative UWB radar approach, for early-stage breast-tumor detection. Several aspects of this approach have been proposed in a series of previous publications [6-8]. The main objective of this article is to provide an overview of the principles, development, and current research status of this UWB imaging approach by integrating the body of published work with some previously unpublished yet useful techniques and results.

Two possible configurations are considered. The first configuration involves the patient lying in the supine (or face-up) position, where an antenna array is placed near the naturally flattened breast. This configuration allows for easier access to smaller breast volumes and tumors adjacent to the chest wall. The second configuration involves the patient lying in the prone (or face-down) position, with the breast extending through an opening in a treatment table. In this position, the antenna array encircles or in some other manner surrounds the pendulous breast. This configuration allows for easier access to the full volume of the breast. Finite-Difference Time-Domain (FDTD) simulations are used to evaluate the efficacy of the MIST beamforming approach for detecting small tumors in anatomically realistic numerical breast models. We also demonstrate the experimental feasibility of UWB microwave detection of breast cancer using a first-generation prototype instrument and simple breast phantoms. The experimental test-bed is designed to emulate the clinical configuration

 ISSN 1045-9243/2005/$20 ©2005 IEEE

where a two-dimensional antenna array is placed near the surface of the naturally flattened breast of a patient lying in the supine position.

The following section provides an overview of UWB microwave breast-cancer detection, including the motivation, advantages, and challenges of the technique. The signal processing and image formation algorithms are presented in Section 3. We demonstrate the effectiveness of these algorithms for breast-tumor detection and localization by applying them to simulated backscattered signals obtained from numerical breast phantoms (Section 4), as well as experimental backscattered signals obtained from physical breast phantoms (Section 5). Concluding remarks follow in Section 6.

2. Background and Motivation for UWB Microwave Breast-Cancer Detection

Breast cancer is one of the leading causes of death among women in the United States. More than 180,000 new cases of invasive breast cancer are diagnosed and more than 40,000 deaths result from the disease each year [15]. Early detection and timely medical intervention are key factors affecting long-term survival and the quality of life of breast-cancer patients. Conventional mammography, which involves X-ray imaging of a compressed breast, remains the primary screening method for detecting non-palpable early-stage breast cancer. Significant technical advances – such as digital mammography, as well as advances in radiological expertise, driven in part by the Mammography Quality Standards Act – have greatly improved the overall quality and interpretation of mammographic images. Despite this progress, persisting limitations related to sensitivity result in a relatively high false-negative rate [16]. Furthermore, the low positive predictive rate of mammography leads to many unnecessary biopsies [17]. Other concerns include uncomfortable or painful breast compression, and exposure to low levels of ionizing radiation. Ultrasound and contrast-enhanced MRI (magnetic resonance imaging) play an important role in the diagnostic evaluation of mammographically detected lesions. However, these modalities are either not yet sensitive/specific enough, too operator dependent, or too costly for screening purposes. The tremendous toll that breast cancer takes, combined with the persisting concerns about X-ray mammography, continue to drive the search for alternative breast-screening tools that image other physical tissue properties or metabolic changes [15]. Microwave breast imaging is one of the promising alternatives under investigation.

Several dielectric spectroscopy studies reported in the literature over the past 20 years [18-20] suggest that the contrast in dielectric properties between malignant and normal breast tissue is greater than 2:1 in the RF and microwave frequency range, as shown in Figure 1. Recognition of the potential diagnostic value of such a contrast is one of the primary motivating factors for the development of electromagnetic imaging technologies for breast-cancer detection. The fundamental difference in the dielectric constant, ε_r, and conductivity, σ, appears to arise in part from the increased water content in neoplastic tissue, due to increased protein hydration [21] and vascularization of the cancerous tissue. Thus, while microwave frequencies do not offer the potential for the fine spatial resolution provided by X-rays, they can exploit strong indicators of malignancy associated with physical or physiological factors of clinical interest, such as water content, vascularization/angiogenesis, blood-flow rate, and temperature.

We note that large malignant-to-normal contrasts in dielectric properties are present across other regions of the electromagnetic spectrum. The contrast at very low frequencies, due in part to the breakdown of necrotic cell membranes, serves as the physical basis for electrical impedance tomography [23, 24], while the contrast at higher (optical) frequencies, due to increased DNA, protein, and hemoglobin absorption in malignant tissue, serves as the physical basis for near-infrared tomography [25]. Our rationale for exploring the use of microwave frequencies is that the 1 to 10 GHz regime balances between the conflicting demands of spatial resolution (better at higher frequencies) and penetration depth (better at lower frequencies). As shown in Figure 1, the contrasts observed at radio frequencies appear to extrapolate out into this desirable microwave frequency range [8].

Two types of active microwave imaging techniques – tomography and radar – have been proposed to exploit this dielectric contrast. In both approaches, low-power microwave signals are transmitted into the breast using an array of antennas, which, in turn, measures the scattered microwave signals. The goal in tomography is to use the scattered signals to recover the profile of the dielectric properties of the breast. Tomographic image reconstruction is most commonly attempted in the frequency domain, using narrowband signals. A non-linear inverse scattering problem must be solved, and iterative image reconstruction algorithms are usually required to obtain a solution. In general, these ill-posed inverse scattering approaches suffer from non-uniqueness, and require regularization in order to achieve convergence to a meaningful solution. However, with smaller geometries, as the case with breast imaging, some of these concerns are minimized. A promising two-dimensional clinical system for microwave breast-imaging research studies has been developed [26]. Significant progress is also being made towards the challenging problem of full three-dimensional image reconstruction [27, 28].

UWB radar techniques do not generally attempt to reconstruct the complete profile of dielectric properties of the breast, but instead seek only to identify the presence and location of significant backscattered energy arising from the dielectric contrast between normal and malignant breast tissue. The scattered signals are processed to generate a map of backscattered microwave energy – or some other measure that provides information of the existence and location of malignant tumors – as a function of spatial location in the breast. MIST beamforming is one type of UWB radar technique that implements spatial filtering to focus microwave signals as a post-processing step, using a beamformer. In this approach, the position of the focus is scanned throughout the breast by adjusting the beamformer for each new focal point. If a scattering object – such as a malignant tumor – exists at the focal point, a relatively large amount of energy is output by the beamformer. Systematic scanning of the synthetic focus from point to point within the breast creates a three-dimensional microwave image of significant scattering points within the internal breast tissue. The beamformer can be as simple as a time-shift-and-sum scheme to create a synthetically focused signal [5, 29]. More advanced least-squares optimal beamformers [30] compensate for frequency-dependent propagation effects, and offer enhanced capability for discriminating against clutter caused by breast-tissue heterogeneity and noise [6, 7].

The expected features associated with microwave breast imaging in general – and more specifically, with UWB space-time microwave imaging for breast-cancer detection – are as follows:

1. Substantial contrasts between the dielectric properties of normal and malignant breast tissue at microwave frequencies

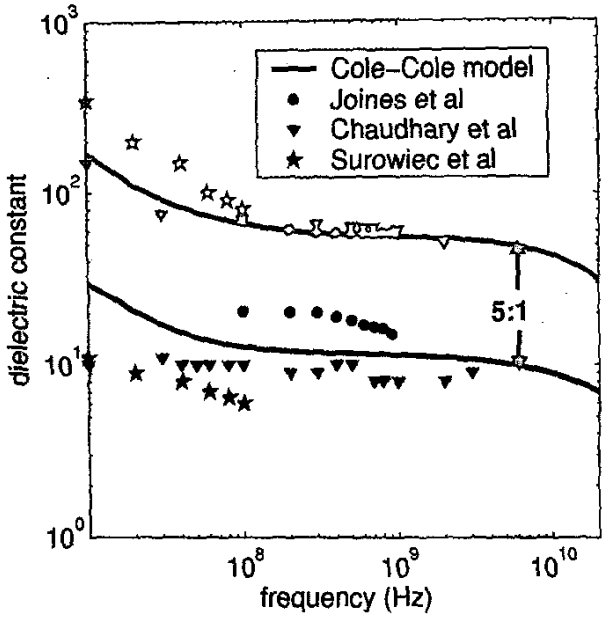

Figure 1a. A summary of measured dielectric constant data for normal and malignant breast tissue at radio and microwave frequencies. Four-term Cole-Cole parametric dispersion models for infiltrated fat (black curve) and muscle (red curve) were used to illustrate the extrapolation of measured data to higher frequencies (above 3 GHz).

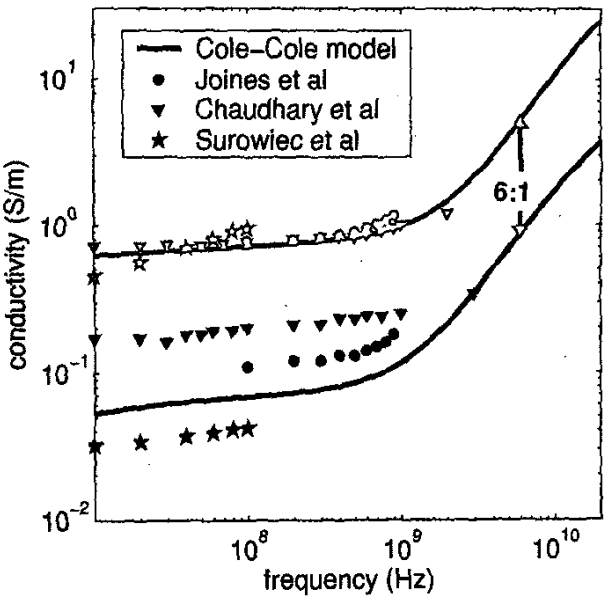

Figure 1b. As in Figure 1a, for the conductivity.

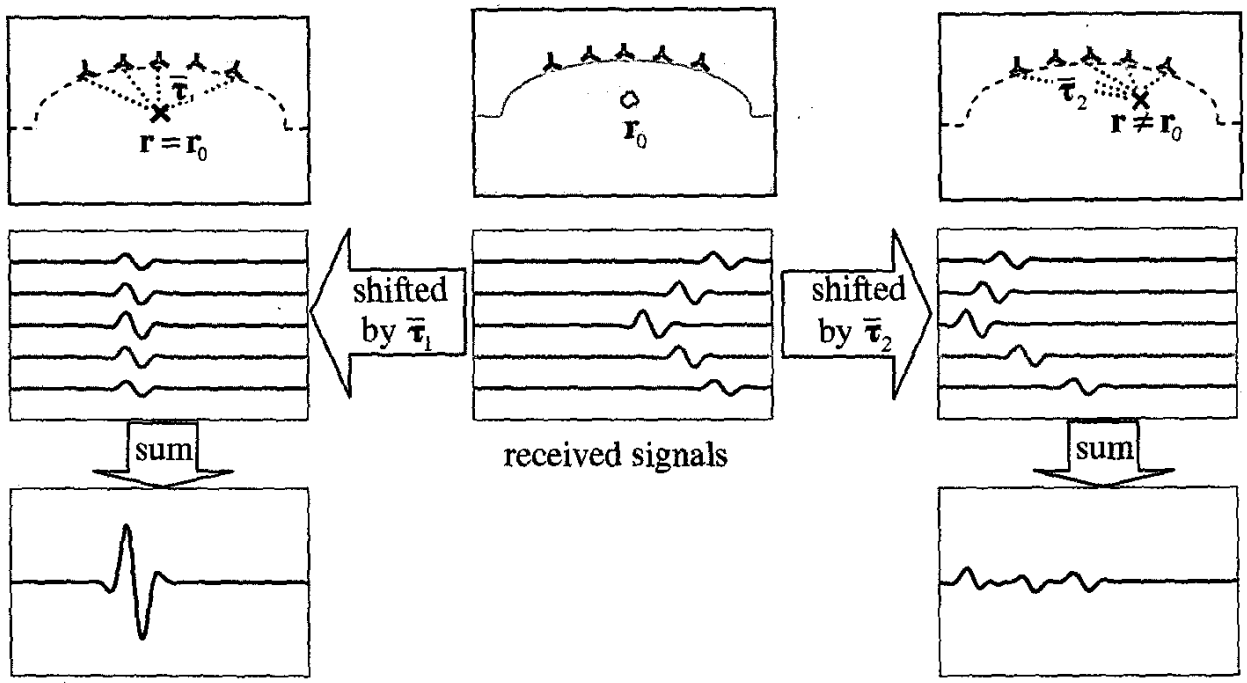

Figure 4. An illustration of simple delay-and-sum beamforming. The received signals are shown in the central panel. When the beamformer is steered to location r_0 (the actual location of a scatterer), the signals coherently sum, as shown by the left panel. When the beamformer is steered to a location other than r_0, incoherent summation results, as shown by the right panel.

have been reported. Consequently, microwaves may offer higher intrinsic tissue contrasts compared to other imaging modalities.

2. Microwave attenuation in normal tissue is low enough to permit imaging of the entire breast.

3. Microwave imaging based on low-power microwave pulses poses no health risk, and avoids breast compression.

4. UWB space-time microwave imaging overcomes the computational challenges of conventional microwave tomography, and permits full three-dimensional imaging.

5. Space-time processing provides the resolution needed to detect and localize (≤ 0.5 cm) malignant tumors. The use of an antenna array and short pulses enable focusing in both space and time, thereby overcoming previous challenges presented by breast heterogeneity, and enabling the detection of lesions as small as 1-2 mm [6].

6. UWB microwave imaging offers the potential for discriminating between malignant and benign lesions. Those benign lesions that exhibit negligible dielectric contrast with normal breast tissue will not act as strong microwave scatterers, in which case they are distinguished from malignant lesions based on backscattered intensity. However, for those benign lesions that mimic malignant lesions in terms of dielectric properties, UWB imaging can exploit morphology-dependent characteristics, such as spectral and polarization signatures, as well as the enhanced backscatter due to vascularization of malignant tumors for the purpose of lesion discrimination and characterization [3].

In summary, we believe that UWB space-time microwave imaging offers the potential of a non-ionizing, non-invasive screening technology that may help reduce the number of false-positives and false-negatives, especially in challenging cases of radiographically dense breast tissue, tumors located near the chest wall, or tumors located near the underarm, where an estimated 50% of all breast lesions occur [31].

Nevertheless, there are several challenges associated with this UWB radar approach. Some of these challenges are common to any microwave breast-imaging modality employing an antenna array. In terms of signal and image processing, imaging resolution on the order of millimeters is desirable for detecting breast cancers in the early stage. Therefore, optimized focusing of the backscattered signals in the post-processing step is required. Furthermore, the mismatch in dielectric properties at the skin-breast interface generates a scattering response at least one order of magnitude larger than any tumor response. The tumor response is further masked by clutter generated by the natural heterogeneity of normal breast, i.e., the variation in dielectric properties between adipose and glandular breast tissues. These artifacts need to be removed or suppressed with minimum distortion of the tumor response. In terms of experimental implementation, the challenges include the design and fabrication of UWB antenna elements and arrays, the management of the aperture size and scan time, etc. In the following sections, we address some of these issues in our discussion of signal processing and experimental techniques, and in the presentation of preliminary results demonstrating the efficacy of the UWB microwave-imaging approach.

3. Signal Processing

This section describes the processing carried out on the set of received signals to obtain an image of backscattered microwave energy. Each received signal contains contributions from antenna reverberations, the skin-breast interface, clutter due to heterogeneity in the breast, backscatter from possible lesions, and noise. Estimating the location of the breast surface using the reflected signals due to the skin-breast interface is described in the first subsection. Subsection 3.2 discusses the removal of the early-time artifacts from each received signal while minimizing distortion to any backscattered tumor response. Delay-and-sum beamforming is reviewed in the third subsection. This section ends with a description of MIST beamforming for enhancing the tumor response while suppressing clutter, allowing for reliable detection and localization of lesions.

3.1 Breast Surface Identification

The relative positions of the surface of the breast and the locations of the antennas are needed to account for propagation effects in the design of high-performance lesion detection and imaging algorithms. This information is unknown *a priori* and is expected to vary from patient to patient. Consequently, we have developed a patient-specific algorithm for estimating the location of the skin-breast interface relative to the antenna locations using recorded backscattered signals. Our approach is based on geometric principles, and the fact that the impedance mismatch at the skin-breast interface results in significant backscatter. First, we apply a matched filter to the backscattered signal in each antenna channel to estimate the propagation time from the antenna to the skin-breast interface. The propagation time locates the skin-breast interface on a sphere with known radius, as shown in Figure 2. Next, we assume that the skin surface is convex and tangent to the sphere. The tangents are found by assuming that the spheres centered at adjacent antennas share the same tangent. This is a very good approximation if the antennas are sufficiently closely spaced relative to the curvature of the breast surface. The skin-breast interface is estimated to be located at the point where the sphere and tangent line touch. Note that multiple tangent points are

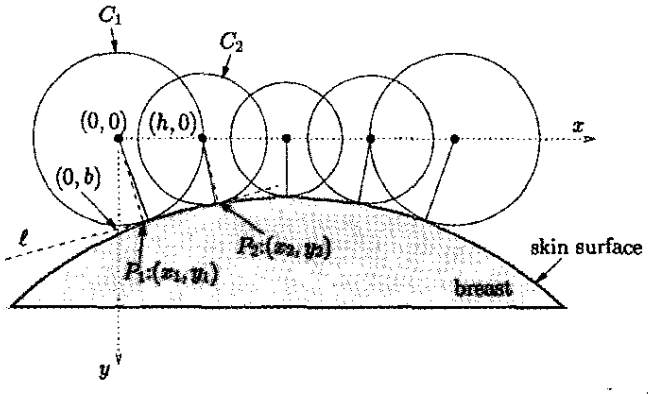

Figure 2. An illustration of the breast-surface (skin-breast interface) estimation algorithm, which is based on the relationship between spheres derived from propagation time estimates and tangents to the surface.

obtained for each interior antenna, because of different pairings with adjacent antennas. In these cases, the average of each tangent point is used as the estimate of the skin-breast interface location.

We now describe how to determine the tangent points for a pair of adjacent antennas in two dimensions. Figure 2 illustrates the adjacent circles, C_1 and C_2, under consideration, and the line, ℓ, tangent to both circles at points $P_1:(x_1,y_1)$ and $P_2:(x_2,y_2)$. Each solid radial line shown in Figure 2 terminates at the point where the skin surface and the circle are tangent. The two dashed radial lines are orthogonal to line ℓ, and indicate that the error between the true and estimated tangent points is small. Letting h denote the inter-element spacing, and r_1 and r_2 denote the radial distances for C_1 and C_2, respectively, the slope of the tangent line to each circle can easily be derived, using calculus, to be $m_1 = \frac{-x_1}{\sqrt{r_1^2 - x_1^2}}$ and $m_2 = \frac{h - x_2}{\sqrt{r_2^2 - (x_2 - h)^2}}$. This allows the equation of the tangent line to each circle to be written as

$$y_1 = m_1 x_1 + b_1 = \frac{-x_1}{\sqrt{r_1^2 - x_1^2}} x_1 + b_1, \quad (1)$$

$$y_2 = m_2 x_2 + b_2 = \frac{h - x_2}{\sqrt{r_2^2 - (x_2 - h)^2}} x_2 + b_2, \quad (2)$$

where b_1 and b_2 are the y intercepts. The constraint of using the line simultaneously tangent to both circles implies that $m_1 = m_2$ and $b_1 = b_2 = b$. Setting $m_1 = m_2$ yields the following relation between x_1 and x_2:

$$x_2 - h = \frac{x_1 r_2}{r_1}. \quad (3)$$

By setting the values of b in Equations (1) and (2) equal to each other, some algebraic manipulation with usage of Equation (3) yields the following equation for x_1:

$$x_1 = \frac{r_1^2 - r_2 r_1}{h}. \quad (4)$$

The y coordinate, y_1, can naturally be calculated using the equation of the circle for C_1.

3.2 Early-Time Artifact Removal

The early-time artifact-removal algorithm presented in this subsection was introduced in [6]. In this subsection, we review the formulation of this method.

Suppose the antenna array has N elements, and denote the received signal at the ith antenna as $b_i(t)$. Each received signal is converted to a sampled waveform, $b_i[n]$. The early-time artifacts in the N channels are expected to be similar but not identical, due to local variations in the skin thickness and the underlying breast heterogeneity, as well as imperfect replications of the antenna-array elements populating the sensor array. The artifact-removal algorithm compensates for this channel-to-channel variation by estimating the artifact in the signal received by a single antenna as a filtered combination of the signals received at all other antenna locations, as shown in Figure 3. The estimate is then removed from

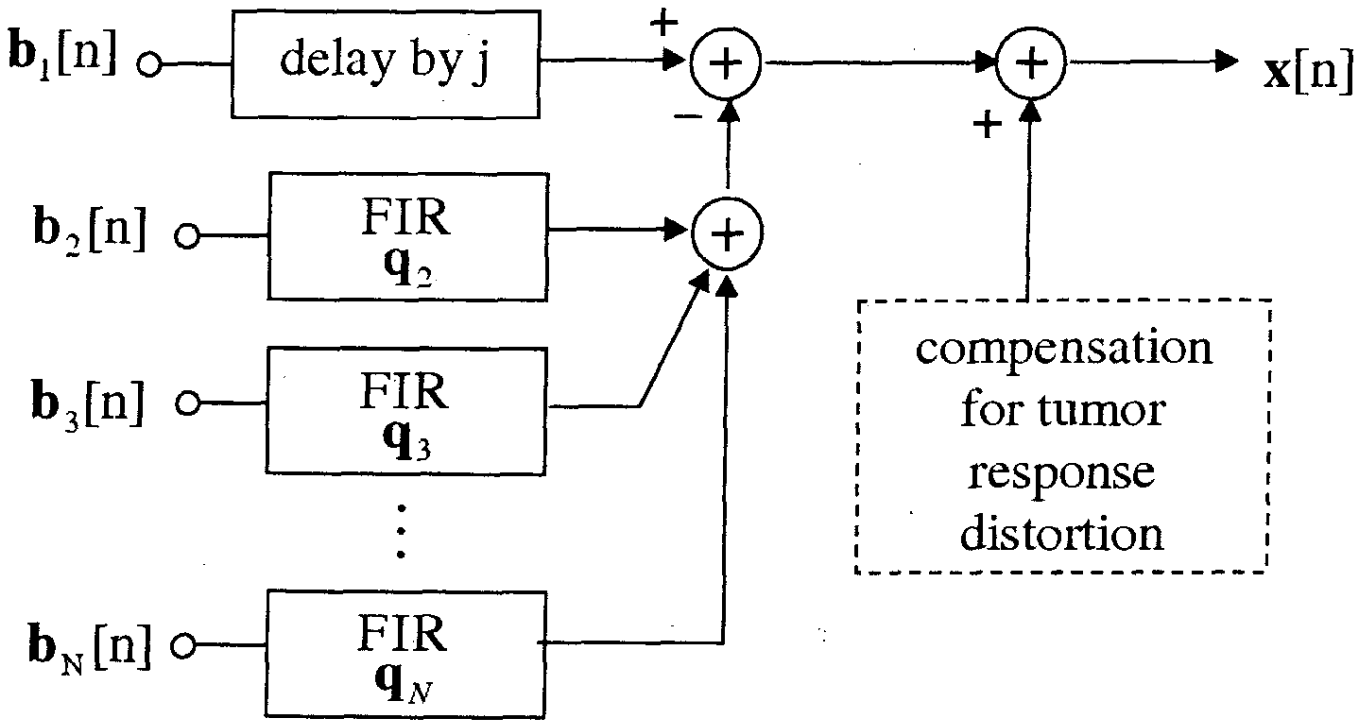

Figure 3. A block diagram illustrating the algorithm for removing the early-time artifact from the backscattered signal received at the first of N antennas.

the received signal. The filter weights used to generate the estimate are chosen to minimize the residual signal mean-squared error over the artifact-dominated early-time response. The estimation and removal process is repeated for all channels. We note that this artifact-removal algorithm uses only the received backscattered signals, and does not require any *a priori* information about the dielectric properties or thickness of the skin, or the dielectric properties of the underlying breast tissue.

Suppose that the skin-breast artifact is to be removed from the first antenna, without loss of generality. The skin-breast response at the nth sample in the first channel is estimated from $2J+1$ successive samples centered on the nth sample in each of the other $N-1$ channels. Define the $(2J+1)\times 1$ vector of time samples in the ith antenna channel to be

$$\mathbf{b}_i[n]=\left[b_i[n-J],\cdots,b_i[n],\cdots,b_i[n+J]\right]^T,\ 2\le i\le N, \quad (5)$$

and let $\mathbf{b}_{2N}[n]=\left[\mathbf{b}_2^T[n],\cdots,\mathbf{b}_N^T[n]\right]^T$ be the concatenation of data in channels 2 through N. Let $\mathbf{q}$ be the filter weight coefficient vector for channels 2 through N. The optimal filter weight vector, $\mathbf{q}$, is chosen to satisfy

$$\mathbf{q}=\arg\min_{\mathbf{q}}\sum_{n=n_0}^{n_0+m-1}\left|b_1[n]-\mathbf{q}^T\mathbf{b}_{2N}[n]\right|^2, \quad (6)$$

where the time interval $n=n_0$ to $n=n_0+m-1$ represents the initial portion of the data record containing early-time artifacts and no backscattered signals from lesions. The solution to this minimization problem is given by [32]

$$\mathbf{q}=\mathbf{R}^{-1}\mathbf{p}, \quad (7)$$

$$\mathbf{R}=\frac{1}{m}\sum_{n=n_0}^{n_0+m-1}\mathbf{b}_{2N}[n]\mathbf{b}_{2N}^T[n], \quad (8)$$

$$\mathbf{p}=\frac{1}{m}\sum_{n=n_0}^{n_0+m-1}\mathbf{b}_{2N}[n]b_1[n]. \quad (9)$$

The fact that there is a high degree of similarity among the skin-breast artifact signals in all N channels results in the sample covariance matrix, $\mathbf{R}$, being ill-conditioned. If $\mathbf{R}$ is ill-conditioned, then the matrix inversion in Equation (7) can result in a solution for $\mathbf{q}$ that has a very large norm and thus amplifies noise. In order to prevent this, we replace $\mathbf{R}$ with a low-rank approximate covariance matrix, obtained using the significant eigenvalues of $\mathbf{R}$. The skin-breast artifact is removed from the entire data record of the first channel to create artifact-free data $x_1[n]$, given by

$$x_1[n]=b_1[n]-\mathbf{q}^T\mathbf{b}_{2N}[n]. \quad (10)$$

This algorithm introduces a small level of distortion in the backscattered signal from the lesion, because the tumor response in the other $N-1$ channels is added back in to the first channel. The distortion is generally small because $\mathbf{q}$ tends to "average" across the N channels, and the tumor responses in the received signals are not aligned in time; thus, they do not add in phase. One quick method for compensating for the tumor-response distortion is to approximate the tumor response in each of these channels by the filtered signals $x_i[n]$, $i=2,...,N$; filter the approximate signals by $\mathbf{q}$; and add the resulting signals to $x_1[n]$.

3.3 Delay-and-Sum Beamforming

A beamformer is a signal processor used in conjunction with an array of antennas. The beamformer output forms a weighted combination of the signals received at each antenna. Usually, the goal of beamforming is spatial filtering, that is, separation of signals that have similar temporal frequency content but originate from different spatial locations [33]. The quintessential beamformer is the delay-and-sum beamformer, which, as the name implies, time delays and sums the received backscattered signals to create a synthetically focused signal. This is explicitly shown at the n^{th} time sample at location $\mathbf{r}_0$ as

$$z[n,\mathbf{r}_0]=\sum_{i=1}^{N}x_i\left[n-\nu_i(\mathbf{r}_0)\right], \quad (11)$$

where $\nu_i(\mathbf{r}_0)=\nu-\text{round}\left[\tau_i(\mathbf{r}_0)/T_s\right]$, T_s is the sampling interval, and x_i is the backscattered signal received at the ith antenna with early-time artifacts removed, as defined in the previous section. The time-delay in the ith channel, $\tau_i(\mathbf{r}_0)$, is computed from the average wave propagation speed and the round-trip distance between the location of the ith antenna, $\mathbf{r}_i$, and location $\mathbf{r}_0$. The quantity ν is an arbitrary integral delay greater than $\max_i \tau_i(\mathbf{r}_0)$ to ensure causality. The position of the focus is scanned throughout the breast by adjusting the distribution of time shifts of the stored backscattered waveforms for each new focal point. If a scattering object, such as a malignant tumor, exists at the focal point, the signals add coherently and a relatively large power results, as shown in the left panel of Figure 4. The right panel illustrates that if scattering objects exist elsewhere, the waveforms add incoherently, and a relatively small power results. Systematic scanning of the synthetic focus from point-to-point within the breast creates a microwave image of significant scattering points within the internal breast tissue. The confocal microwave-imaging method described in [5, 29] is based on the delay-and-sum beamforming method described here. In three dimensions, this method accounts for the radial spreading produced by the propagating signal (the $1/r$ factor) along with the time of flight.

3.4. MIST Beamforming

The confocal microwave-imaging approach illustrates the significant potential of backscatter-based imaging methods for detecting breast lesions. However, the simple sum-and-time-shift techniques do not allow for compensation of frequency-dependent propagation effects, such as dispersion, and offer limited capability for discriminating against artifacts and noise. Dispersion is important since it can introduce considerable broadening of the transmitted-pulse duration, thereby reducing resolution. We choose to compensate for these frequency-dependent propagation effects by using a broadband beamformer we term the MIST beamformer. In general, a broadband beamformer implements frequency-depend-

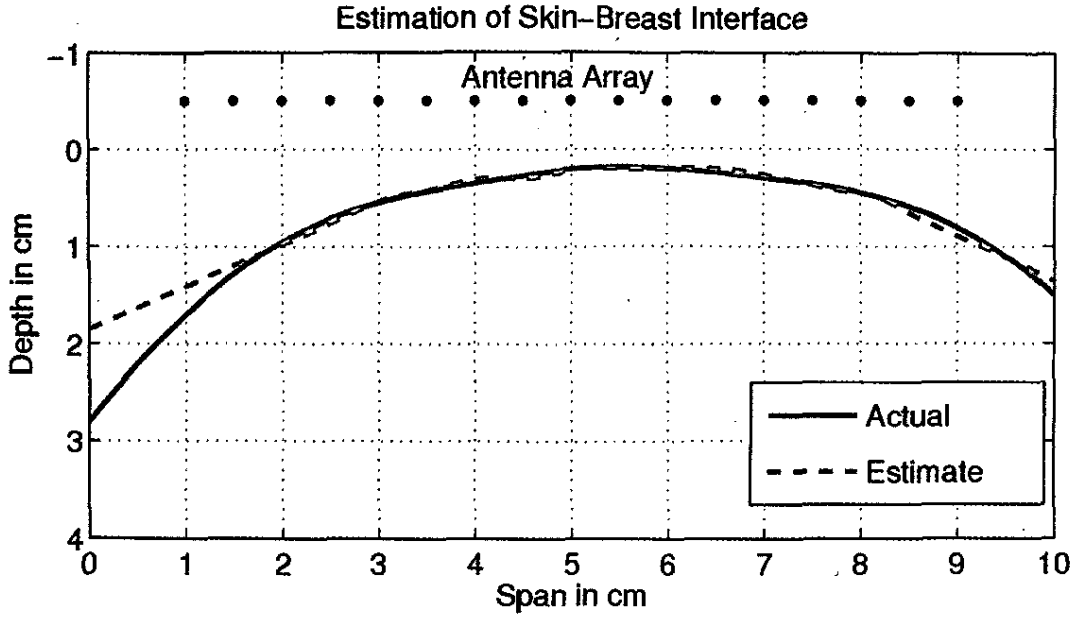

Figure 7. The estimated (red curve) skin-surface contour for the sagittal plane of the supine configuration, obtained by applying the skin-surface-estimation algorithm illustrated by Figure 3. The actual skin-surface contour is shown by the blue curve, for comparison.

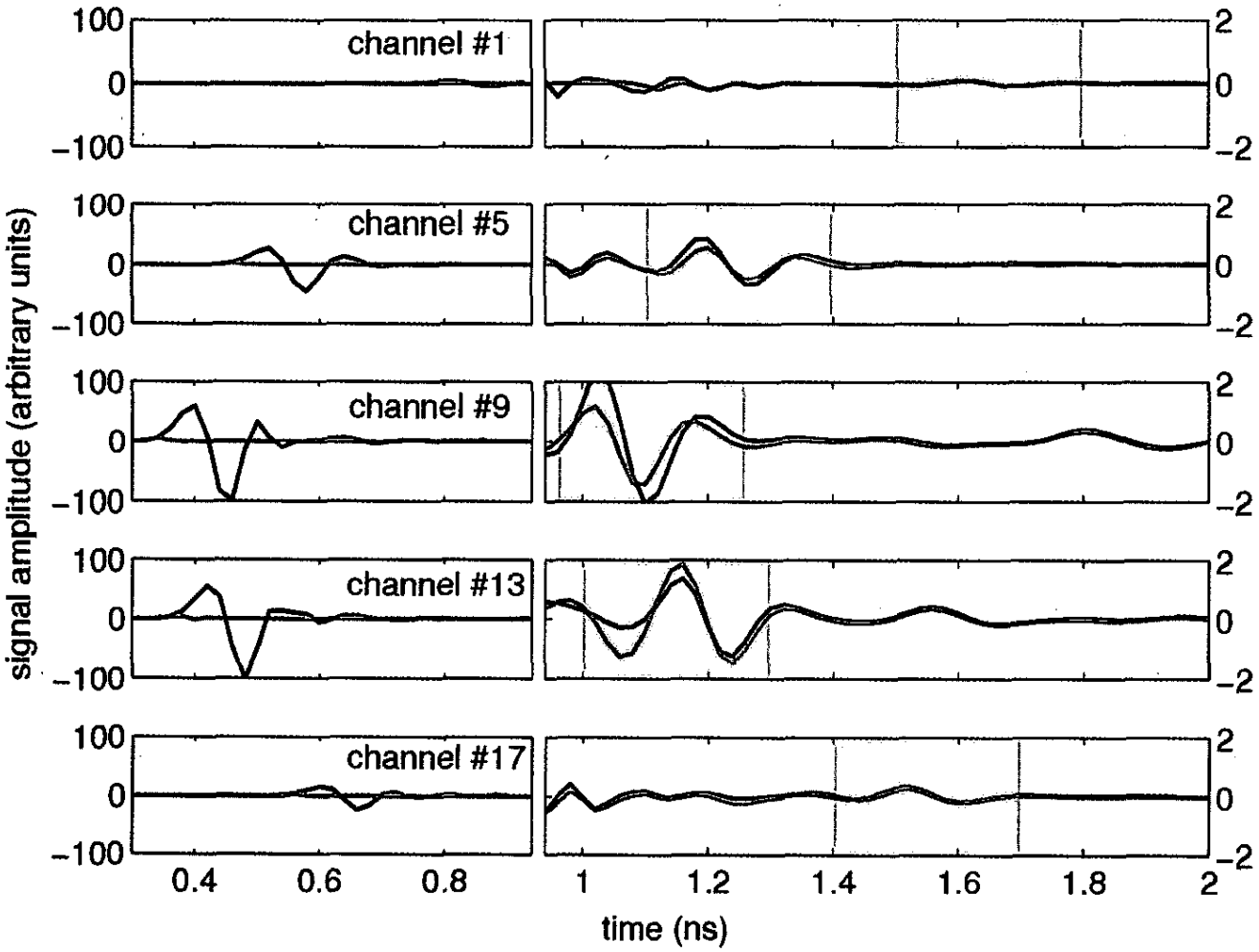

Figure 8. FDTD-computed backscattered signals before (black curves) and after (red curves) applying the skin-breast artifact-removal algorithm. The left panel shows the early-time response, while the right panel shows the late-time response. The shaded regions highlight the expected time window of the tumor response.

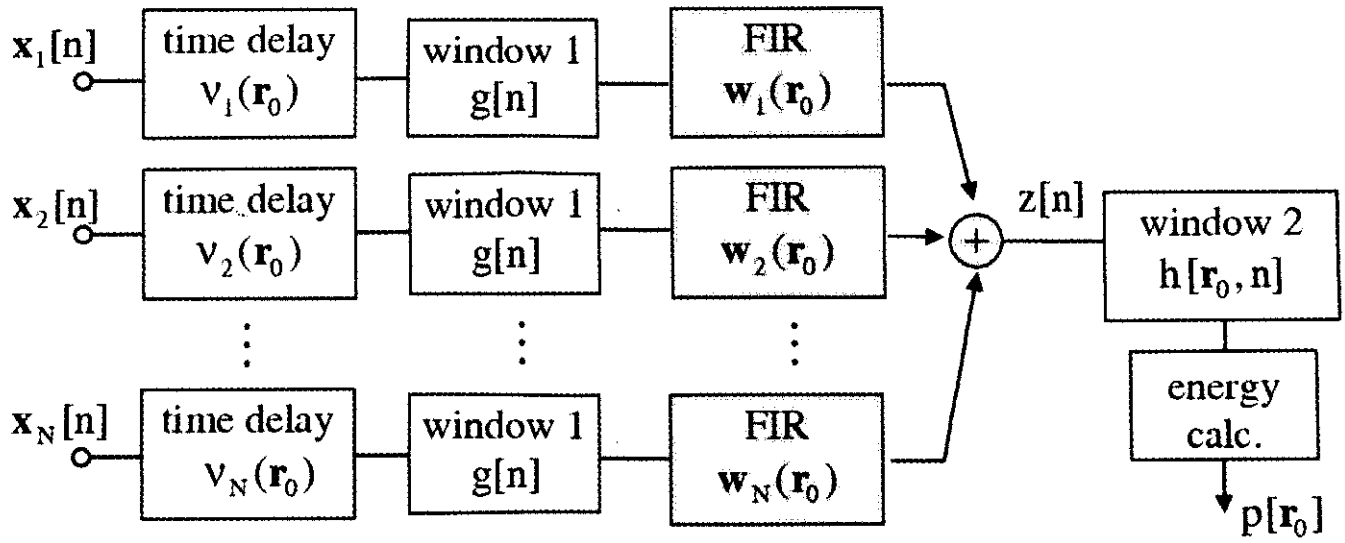

ent amplitude and phase adjustments in each channel. The amplitude and phase shifts can be applied to the data by transforming the data into the frequency domain, or can be implemented in the time domain using a finite-impulse-response (FIR) filter. The output of the time-domain broadband beamformer can be expressed, in general, as

$$z[n,\mathbf{r}_0]=\sum_{i=1}^{N}\sum_{p=0}^{P-1} w_{ip}^{*}x_i\left[n-p-\nu_i(\mathbf{r}_0)\right], \qquad (12)$$

where P is the total number of weights in each channel, and x_i has already been defined. Analogously to Equation (11), Equation (12) shows that broadband beamforming also performs spatial discrimination with the array. The weighted combination of time-delayed versions of each received signal in Equation (12) signifies the frequency-dependent nature of the beamformer. The broadband beamformer given by Equation (12) is a common signal-processing tool in radar, sonar, acoustics, seismology, and communication systems.

The block diagram depicted in Figure 5 shows the MIST beamforming procedure used after artifact removal to reconstruct the image-pixel value for a single pixel location, $\mathbf{r}_0$. This procedure is based on the assumed propagation model for breast tissue, and is repeated for each pixel in the reconstructed image. The signals are first coarsely time-aligned with a delay of $\nu_i(\mathbf{r}_0)$ in each of the N channels, $i=1,2,...,N$. The signals then pass through the MIST beamformer for the purpose of equalizing the transmitted pulse, equalizing path-length- and frequency-dependent phase shifts and attenuation, and performing spatial discrimination against clutter. If a scatterer is located at $\mathbf{r}_0$, the beamformer output is a distorted version of a bandlimited impulse. This waveform has its energy concentrated in a time interval that is inversely proportional to signal bandwidth. We exploit the short duration of the response to discriminate against clutter by calculating energy over a rectangular window centered about the sample, where the peak amplitude occurs when a point scatterer is at $\mathbf{r}_0$. This energy is the pixel value for location $\mathbf{r}_0$.

The design of the space-time beamformer can be performed in the time domain [6] or in the frequency domain [7]. We choose the frequency-domain approach, as it requires substantially less computation than that required by the time-domain approach. The following highlights the frequency-domain beamformer design, and we refer the reader to [7, 34] for additional details. Let $I(\omega_k)$ be the discrete Fourier transform (DFT) of the transmitted UWB pulse, where ω_k is the frequency corresponding at the kth discrete Fourier transform index. Let $S_{ii}(\omega_k,\mathbf{r}_0)$ be the monostatic frequency response associated with propagation through breast tissue from the ith antenna to the scatterer located at $\mathbf{r}_0$, and back. We represent the frequency response remaining after factoring the linear phase shift associated with average round-trip propagation delay out of $S_{ii}(\omega_k,\mathbf{r}_0)$ by $\tilde{S}_{ii}(\omega_k,\mathbf{r}_0)$. Denote the beamformer weight in the ith channel at discrete-Fourier-transform index k as $W_i[k,\mathbf{r}_0]$. The beamformer is designed only at the frequencies that lie in the UWB pulse band, and is set to zero at frequencies that lie outside of this band. Now, form the respective $N\times 1$ column vectors,

$$\mathbf{v}(\omega_k,\mathbf{r}_0)=\left\{I(\omega_k)\tilde{S}_{ii}(\omega_k,\mathbf{r}_0)\right\}_{i=1}^{N}$$

and

$$\mathbf{w}(\omega_k,\mathbf{r}_0)=\left\{W_i[k,\mathbf{r}_0]\right\}_{i=1}^{N}.$$

Since the beamformer is designed to compensate for round-trip propagation to and from location $\mathbf{r}_0$, we require the combined effects of the coarse time alignment and propagation to have unit gain and linear phase. This is explicitly shown by the first term in the penalized least-squares problem

$$\mathbf{w}(\omega_k,\mathbf{r}_0)=\arg\min_{\mathbf{w}}\left|\mathbf{w}^H(\omega_k,\mathbf{r}_0)\mathbf{v}(\omega_k,\mathbf{r}_0)-e^{-j\omega_k\tau_0}\right|^2 + \xi\mathbf{w}^H(\omega_k,\mathbf{r}_0)\Lambda[k,\mathbf{r}_0]\mathbf{w}(\omega_k,\mathbf{r}_0), \qquad (13)$$

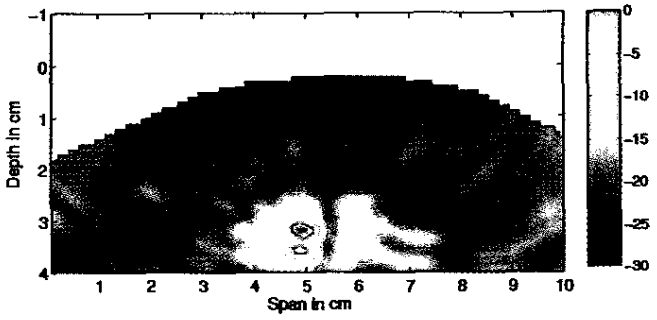

Figure 9. Color images showing the backscattered energy on a dB scale for the two-dimensional numerical breast phantoms of Figure 6. A 2-mm-diameter malignant tumor was centered at (a) (5.0 cm, 3.1 cm) for the supine configuration, and (b) (2.0 cm, 4.0 cm) for the prone configuration. Both image-reconstruction regions were masked using estimated skin-surface contours.

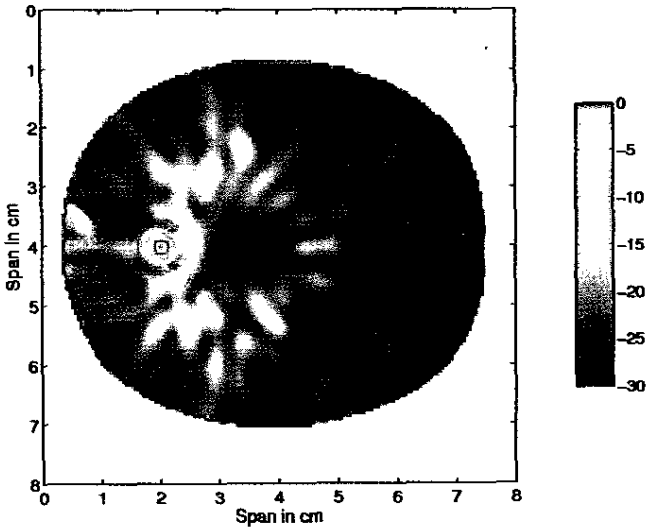

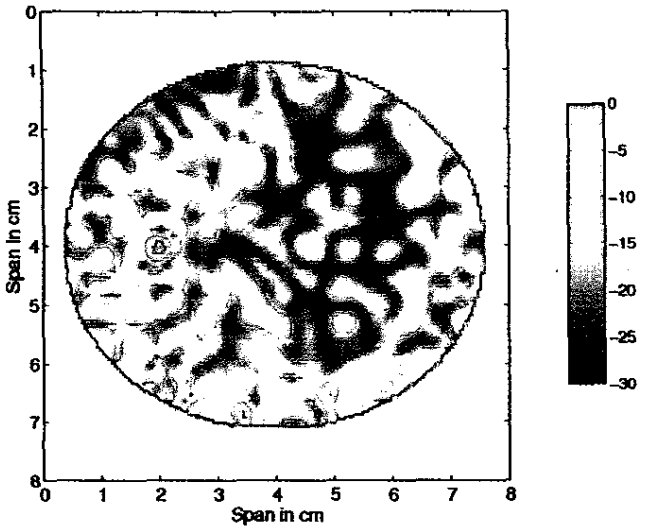

Figure 10a. A color image showing the backscattered energy on a dB scale for a numerical breast phantom similar to Figure 6b when the idealized artifact removal algorithm was used to preprocess the received signals. The average dielectric properties of normal breast tissue are $\varepsilon_r = 15.7$ and $\sigma = 1.0$ S/m at 6 GHz.

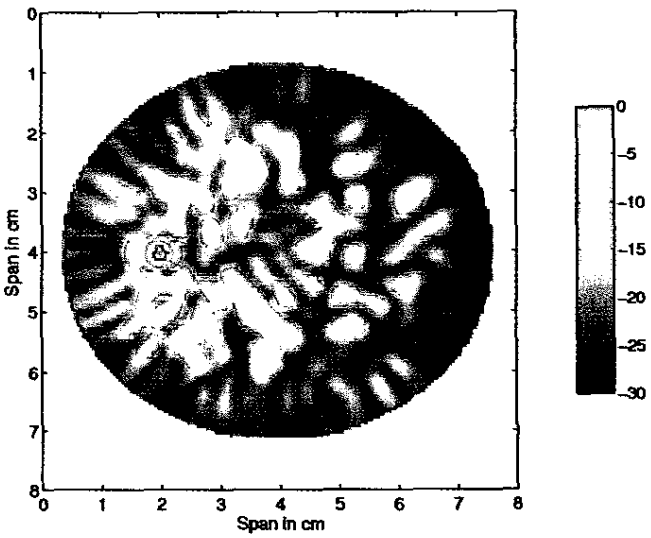

Figure 10b. A color images showing the backscattered energy on a dB scale for a numerical breast phantom similar to Figure 6b when the early-time artifact removal algorithm was used to preprocess the received signals. The average dielectric properties of normal breast tissue are $\varepsilon_r = 15.7$ and $\sigma = 1.0$ S/m at 6 GHz.

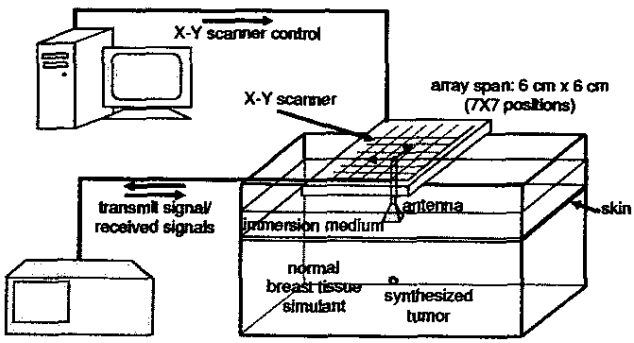

Figure 11a. An illustration of the experimental system setup.

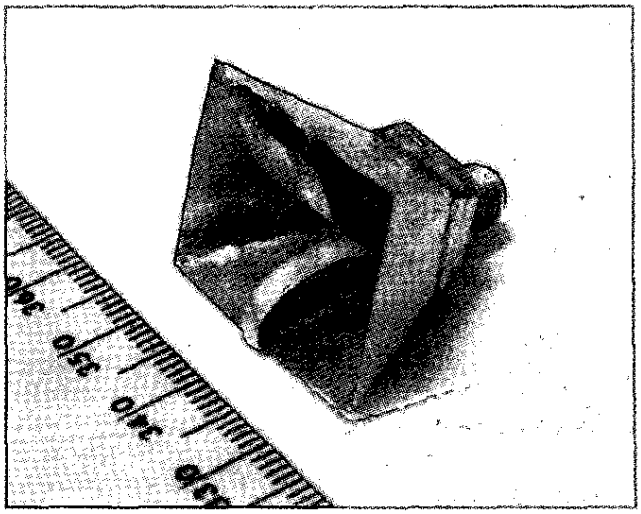

Figure 11b. The miniaturized pyramidal horn with a single ridge and curved launching plane terminated with chip resistors, used as the UWB antenna.

where $\tau_0 = T_s(M-1)/2$ is the average time delay introduced by the length-M FIR filters, assuming a sampling interval T_s. The second term of Equation (13) controls the noise gain, and makes the beamformer more robust to errors between the actual and assumed propagation model. The quantity $\Lambda[k,\mathbf{r}_0]$ is a matrix representing the structure of the penalty, and ξ is a real non-negative parameter the value of which is selected to scale the impact of the penalty. The matrix $\Lambda[k,\mathbf{r}_0]$ is chosen to be a diagonal matrix with entries $\left\{\left|I(\omega_k)\tilde{S}_{ii}[k,\mathbf{r}_0]\right|\right\}_{i=1}^{N}$, as this offers a balance between white noise gain and sensitivity to tissue-propagation errors [34]. Using this choice for the penalty, the solution to Equation (13) is obtained as

$$W_i[k,\mathbf{r}_0] = \frac{\tilde{S}_{ii}[k,\mathbf{r}_0]e^{j\omega_k\tau_0}}{\left|\tilde{S}_{ii}[k,\mathbf{r}_0]\right|\left(\xi + \sum_{m=1}^{N}\left|\tilde{S}_{mm}[k,\mathbf{r}_0]\right|\right)}. \qquad (14)$$

The filter tap weights in the ith channel, w_{ip} (see Equation (12)), $p = 0,\ldots,P-1$, are obtained by performing the inverse discrete Fourier transform of $W_i[k,\mathbf{r}_0]$.

We now consider the specific beamformer designs used to generate the results presented in this article. In the case of the two-dimensional numerical breast phantoms discussed below in Section 4, the antenna array was assumed to have $N = 17$ elements. The transmitted UWB pulse was a differentiated Gaussian, with full-width at half maximum equal to 110 ps. The discrete Fourier transforms used $M = 125$ samples, and the beamformers were designed for the 28 frequencies that were in the UWB-pulse band. We set ξ to be 1. The propagation model used in the two-dimensional design of the beamformer assumed transmission through two uniform dielectric media: a coupling medium consisting of skin, and normal breast tissue. Note that the malignant breast-tissue medium was not included in the propagation model. The antenna array was located in the coupling medium near the breast medium. An estimate of the minimum distance, d_{c_i}, the UWB pulse traveled in the coupling medium from the ith antenna to the breast surface is obtained when carrying out the skin-surface estimation algorithm. For any location, $\mathbf{r}$, in the breast region, we assume that the distance the pulse travels in the breast, $d_{b_i}(\mathbf{r})$, is given by the distance from the ith antenna to location $\mathbf{r}$ minus the estimated distance the UWB pulse travels in the coupling medium,

$$d_{b_i}(\mathbf{r}) = |\mathbf{r} - \mathbf{r}_i| - d_{c_i}, \qquad (15)$$

where $\mathbf{r}_i$ is the location of the ith antenna. The monostatic frequency response, $S_{ii}(\omega,\mathbf{r})$ incorporates the frequency-dependent propagation effects in the coupling medium and normal breast tissue, explicitly shown by the product of two quantities in the following equation:

$$S_{ii}(\omega,\mathbf{r}) = \left[\frac{1}{\sqrt{d_{c_i}}}e^{-\alpha_c(\omega)d_{c_i}}e^{-j\beta_c(\omega)d_{c_i}}\right]^2 \cdot \left[\frac{1}{\sqrt{d_{b_i}(\mathbf{r})}}e^{-\alpha_b(\omega)d_{b_i}(\mathbf{r})}e^{-j\beta_b(\omega)d_{b_i}(\mathbf{r})}\right]^2, \qquad (16)$$

where $\alpha_c(\omega)$ and $\alpha_b(\omega)$ are the frequency-dependent attenuation constants in the coupling medium and the breast, respectively, and $\beta_c(\omega)$ and $\beta_b(\omega)$ are the frequency-dependent phase constants in the coupling medium and breast, respectively. A far-field approximation is inherent in Equation (16). Although this propagation model involves several simplifying assumptions, we show in the next section that this model results in designs that are effective in realistic scenarios.

In the three-dimensional experimental scenario discussed in Section 5, the antenna array was assumed to have $N = 49$ antennas. The discrete Fourier transforms used 62 samples, and the beamformer weights were designed at 17 frequencies. The transmitted UWB pulse was a modulated Gaussian with full-width at half maximum equal to 110 ps. We set $\xi = 1$. The propagation model in the three-dimensional design assumed transmission through a uniform breast-tissue medium, only. There, the malignant breast-tissue medium and the skin medium were not included in the model. The monostatic frequency response was given by

$$S_{ii}(\omega,\mathbf{r}) = \left[\frac{1}{|\mathbf{r}-\mathbf{r}_i|}e^{-\alpha|\mathbf{r}-\mathbf{r}_i|}e^{-j\beta|\mathbf{r}-\mathbf{r}_i|}\right]^2, \qquad (17)$$

where the attenuation factor, α, and the phase constant, β, were constants evaluated at the spectral peak of the input signal.

4. Results for Numerical 2-D Phantom

In this section, we demonstrate the effectiveness of the MIST beamforming algorithms by applying them to simulated backscattered data computed using the FDTD method [35]. This approach allows for rapid evaluation of the performance of the algorithms. First, we review the two-dimensional anthropomorphic numerical breast model used to compute the set of backscattered signals. Then, we show a result that illustrates the accuracy of the skin-breast-interface estimation algorithm. Next, we discuss the results of applying the artifact-removal algorithm to the received backscattered signals. Lastly, we present and discuss images generated by passing backscattered signals through the space-time beamformer.

4.1 Two-Dimensional Numerical Breast-Phantom Development

A two-dimensional TM_z FDTD-based electromagnetic model was used to investigate the effectiveness of our MIST beamforming strategy. The FDTD electromagnetic model solved Maxwell's equations on a discrete spatial grid, comprised of a numerical breast phantom and an antenna array configuration. The supine and prone positions were considered. In both configurations, the breast was immersed in a coupling medium matched to the skin layer. In the supine configuration, a uniform linear array was placed near the surface of the naturally flattened breast. In the prone configuration, an elliptical array encircled the pendulous breast.

To approximate the supine configuration in two dimensions, we considered a sagittal plane through the breast, with antennas positioned near the top of the breast, as shown in Figure 6a. The

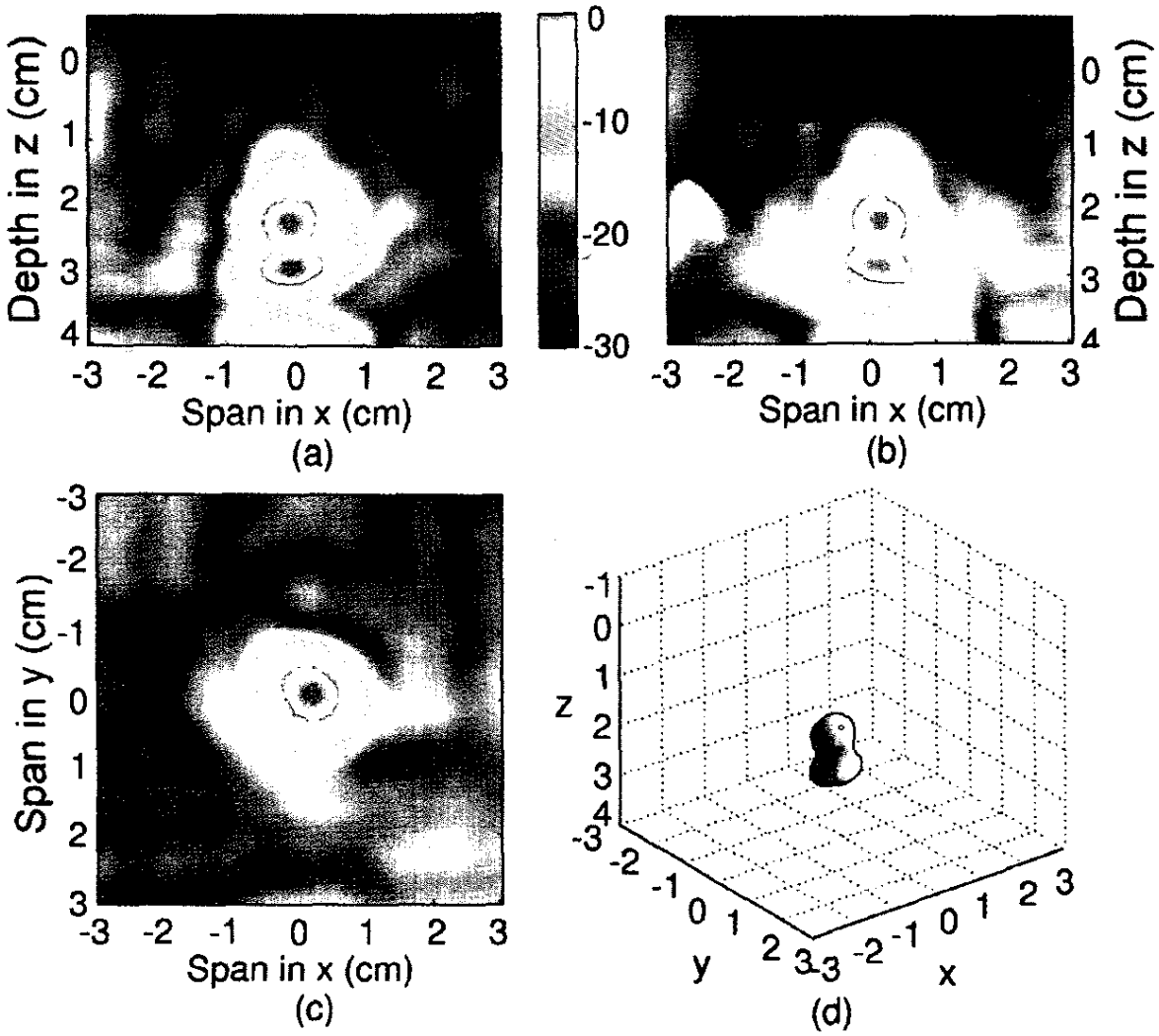

Figure 12. Color images of backscattered energy for the experimental breast phantom, which contained a 4-mm-diameter synthetic tumor located at a depth of 2 cm below the skin surface. The contrast in ε_r between normal and malignant tissue simulants was only 1.5:1. The orthogonal planes intersect the shallower of the two energy peaks of the tumor response: (a) yz plane at $x = 0.1$ cm, (b) xz plane at $y = 0.1$ cm, (c) xy plane at $z = 2.3$ cm, (d) a three-dimensional image showing the -3 dB contour for this particular breast phantom.

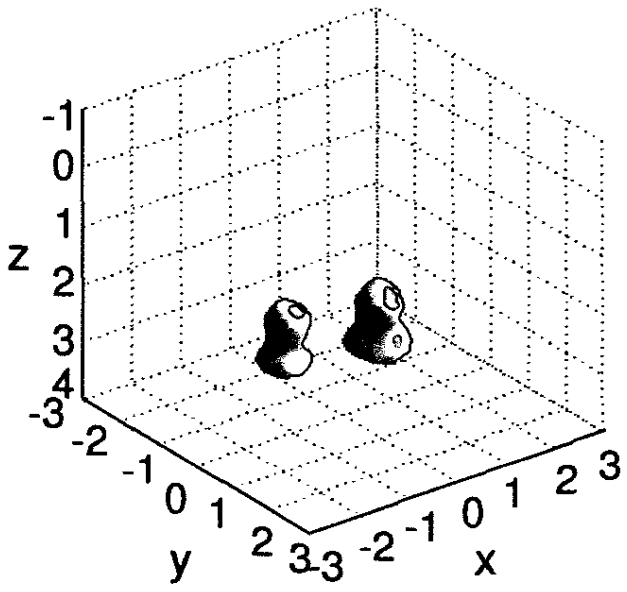

Figure 13. A three-dimensional image showing the -3 dB contour for the experimental breast phantom, which contained two 4-mm-diameter synthetic tumors located at a depth of 2 cm below the skin surface, with a lateral distance of 2 cm between each tumor.

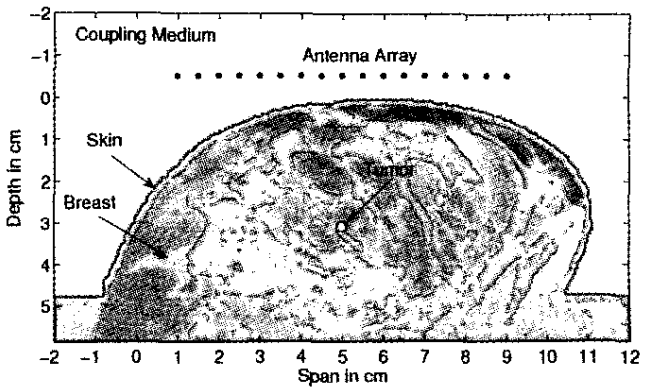

Figure 6a. A two-dimensional MRI-derived FDTD breast model for a patient lying in the supine position. The model contains a 2-mm-diameter malignant lesion, shown by the white dot. The 17 black dots away from the surface of the breast represent antenna locations.

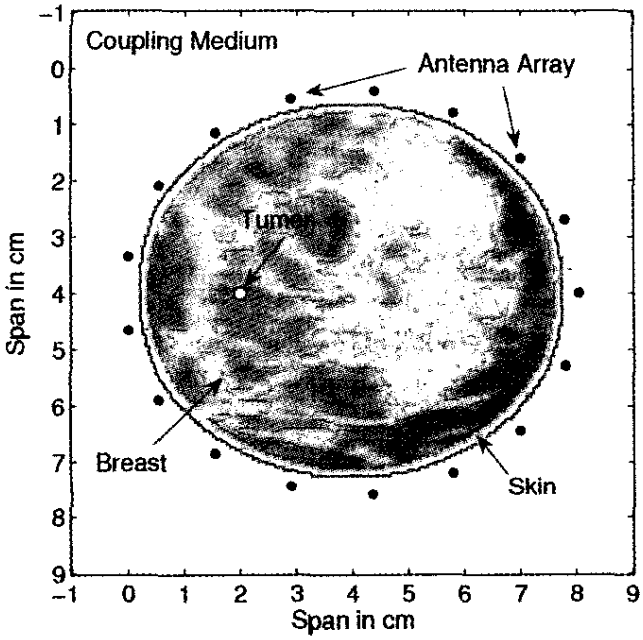

Figure 6b. A two-dimensional MRI-derived FDTD breast model for a patient lying in the prone position. The model contains a 2-mm-diameter malignant lesion, shown by the white dot. The 17 black dots away from the surface of the breast represent antenna locations.

grayscale display of the interior of the breast shows the anatomically realistic variation of the permittivity within the breast, which was derived from the density variation of a high-resolution breast MRI data set. Here, lighter regions represent higher dielectric-property values of denser fibroglandular tissue, while the darker regions represent lower dielectric-property values of less-dense adipose tissue. To approximate the prone position in two dimensions, we considered a coronal plane through the breast with antennas surrounding the breast, as shown in Figure 6b. We note that the between-plane resolution of the original three-dimensional MRI data set was lower than the in-plane resolution. Since the in-plane scans corresponded to the sagittal plane, it was the coronal plane that was affected by the lower between-plane resolution. This explains why there was a slight decrease of clarity in the coronal image. The spatial distributions of the dielectric constant shown in Figure 6 are displayed at 6 GHz.

The dispersive properties of breast tissue were also included in our FDTD breast models. The frequency-dependent tissue properties were incorporated in a manner similar to that presented in [5]. For the average properties of normal fatty breast tissue in the model of Figure 4a, the dispersion model yielded $\varepsilon_r = 9.8$ and $\sigma = 0.4$ S/m at 6 GHz, the spectral peak of the ultra-wideband input pulse. At any given frequency, the actual dielectric properties of normal breast tissue vary about the average properties by as much as ±10%, depending on local tissue type and density. The average dielectric properties for malignant breast tissue are $\varepsilon_r = 50.7$ and $\sigma = 4.8$ S/m at 6 GHz.

A 2-mm-diameter malignant tumor was inserted into each breast model. In the sagittal model of Figure 6a, the tumor is shown in a central location in the breast at a depth of 3.1 cm below the surface of the breast. In the coronal model of Figure 6b, the tumor is shown to be at an off-center location in the breast, at a distance of at least 2 cm from the surface of the breast. Thus, each model was composed of three different media: heterogeneous normal breast tissue, skin, and malignant tumor.

4.2. Breast-Surface Identification Result

Figure 7 depicts a two-dimensional example illustrating the performance of the breast-surface identification algorithm when the patient was in the supine position. The red curve represents the estimate of the skin surface, while the blue curve represents the actual skin surface. Note that a cubic B-spline was fit through the estimated tangent points to approximate the skin surface. There was excellent agreement between the estimated and actual interface, although accuracy suffered outside the array aperture, as expected. Similar-quality results were obtained in the prone configuration.

4.3. Early-Time Artifact-Removal Result

We illustrated the efficacy of the early-time artifact removal algorithm using backscattered signals collected from the numerical breast phantom illustrated in Figure 6a. A subset of the received signals ($b_i[n]$ and $x_i[n]$, where $i = 1,5,9,13,17$) are plotted in the left (early-time) and right (late-time) panels of Figure 8. Prior to applying the artifact-removal algorithm, the early-time response, shown by the black curves in the left panel, was dominated by the skin-breast backscattered response. The late-time response, shown by the black curves in the right panel using an enlarged vertical scale, contains the tumor response and clutter due to heterogeneity in the breast. The red curves represent the processed signals, $x_i[n]$, obtained by applying the artifact-removal algorithm assuming $J = 3$, $p = 15$, and $m = 20$. The early-time artifact was almost completely eliminated, as shown in the left panel. The tumor response was preserved, as is evident in the later-time tumor response depicted in the right panel. The shaded areas highlight the time window in which the tumor response was expected, based on the known material properties and location of the tumor. Similar efficacy has been demonstrated with the numerical breast phantom for the prone configuration.

Our algorithm is data adaptive, and is thus able to compensate for variability in the early-time artifacts due to breast heterogeneity. An alternative algorithm for removing early-time artifacts is channel-by-channel subtraction of the backscattered signal recorded from a tumor-free homogeneous breast phantom. This alternative algorithm represents ideal removal of early-time artifacts only if the breast under examination is approximately homogeneous near the skin surface. If the density of the underlying tissue varies greatly throughout the region near the breast surface, as is expected in a practical setting, the assumption of homogeneity is clearly violated, and the idealized algorithm will not effectively remove early-time artifacts from the backscattered signals. The breakdown of the idealized algorithm and the success of our approach is most clearly evident when viewing images of backscattered energy as a function of location. Therefore, these effects are demonstrated at the end of the next subsection.

4.4 MIST Beamforming Results

Figure 9a depicts the scanned beamformer output energy for the breast model of Figure 6a containing the malignant tumor centered at (5.0, 3.1). The coordinates refer to (span, depth) in cm. The energy is displayed in the region beneath the estimated location of the skin-breast interface. The low-level energy spatially distributed throughout the image consisted of the response from the normal heterogeneity and minor distortions introduced by the early-time artifact-removal algorithm. The dominant energy attributed to the tumor response is clearly detectable, as it stands 16 dB above the maximum clutter. We determined the maximum clutter level from the central 6-cm × 2-cm region of the reconstructed image for a tumor-free breast model, and defined the maximum signal-to-clutter (S/C) ratio as the ratio of the peak energy to the maximum clutter energy. The maximum energy occurred at (5.0, 3.2), and the −3 dB radius was approximately 4 mm. Figure 9b depicts the scanned beamformer output energy for the breast model of Figure 6b containing the malignant tumor located at (2.0, 4.0). The coordinates refer to (span, span) in cm. For this coronal plane, the energy is displayed inside the region bounded by the estimated location of the skin-breast interface. The peak energy in the image occurred exactly at the center of the tumor. The −3 dB radius was approximately 2 mm, and the S/C was 20 dB. We determined the maximum clutter level for this configuration from the central 5-cm × 3-cm region of the reconstructed image for a tumor-free breast model. The resolution for the prone configuration was higher, as expected, since the array aperture spanned both dimensions, unlike the array for the supine configuration.

We have found that the MIST beamformer designs consistently produce high-quality images, even under challenging conditions such as varying tumor sizes, variations in breast heterogeneity, and mismatch between assumed and actual dielectric properties of normal breast tissue. These challenging conditions were investigated in [6] for the supine configuration, with the antenna array conformal to the skin surface.

Finally, we compared the performance of the early-time data-adaptive artifact-removal algorithm with the idealized artifact-removal algorithm for the case when both the average density and variability about the average density of the breast model in Figure 6b were increased. This created a more heterogeneous region just beneath the skin surface. Now, the average dielectric properties at 6 GHz were $\varepsilon_r = 15.7$ and $\sigma = 1.0$ S/m, and the variability about the averages was ±30%. Figure 10a shows the image of the beamformer output energy when the idealized algorithm was used for early-time artifact removal, while Figure 10b shows the resulting image when our artifact-removal algorithm was employed. It is quite clear from visual inspection of both images that our early-time artifact-removal algorithm resulted in less detected energy near the breast surface than the so-called idealized algorithm. The ratio of average surface energy (determined from data in a 0.5-cm thick layer beneath the breast surface) to peak tumor energy for the image of Figure 10a was −11.5 dB, whereas the ratio for the image of Figure 10b was −24 dB. This reduction enhanced the detectability of tumors near the surface. Note that breast heterogeneity shows considerable variability, and may be significantly greater than that assumed in this example. Data-adaptive artifact-removal strategies such as ours are very important in highly heterogeneous scenarios.

5. Experimental Investigation of the Supine Configuration

The theoretical feasibility of MIST beamforming for tumor detection has been demonstrated in the previous sections by applying two-dimensional space-time beamformers to simulated backscattered data obtained from MRI-derived two-dimensional FDTD breast models. In this section, we highlight the experimental feasibility of this approach by presenting imaging results of multilayer breast phantoms using our first-generation experimental prototype [8].

The experiment setup shown in Figure 11a emulated a system configuration where a patient was lying in a supine position with a two-dimensional antenna array placed near the surface of the naturally flattened breast. The breast phantom consisted of a container filled with a liquid mimicking normal breast tissue, a small synthetic tumor suspended in the liquid, and a thin layer of material representing the skin layer covering the normal breast-tissue simulant. We designed and fabricated an ultra-wideband antenna to serve as the microwave transmitter and receiver [36]. As shown in the photograph of Figure 11b, this UWB antenna was comprised of a miniaturized pyramidal horn with a single ridge and curved launching plane terminated with chip resistors. The UWB antenna was sequentially repositioned in the horizontal plane using a computer-controlled mechanical x-y scanner to synthesize a two-dimensional antenna array placed above the skin. The antenna was immersed in a matching medium to couple microwave energy into the breast more efficiently. For simplicity, the liquid used for normal breast-tissue simulation was also used as the immersion medium.

Soybean oil was used as the normal breast-tissue simulant in this initial experimental demonstration, since it has dielectric properties similar to very low-water-content fatty tissue. We note that the dielectric properties of the oil ($\varepsilon_r = 2.6$ and $\sigma = 0.05$ S/m at 6 GHz), as measured using an open-ended coaxial-probe technique [37], fell slightly below the expected range of the dielectric properties for fatty breast tissue. Therefore, we chose materials for the skin and tumor simulants that similarly underestimated the actual dielectric properties of those tissue types, so that the dielectric contrasts in the breast phantom were representative of those for actual tissue.

The malignant-tissue simulant, with appropriate ε_r and conductivity, σ, was formed using a diacetin-water solution. The

resulting contrast in ε_r between malignant and normal-tissue simulants was 1.5:1. This contrast was chosen to fall on the lower end of the range of contrasts expected in clinical scenarios. The synthetic tumor was made by pouring the water-diacetin mixture into a 4-mm-diameter cylindrical container that had a height of 4 mm. The container was composed of a section of plastic tube, wrapped and sealed with a latex membrane. The dielectric properties of the container materials were similar to those of the soybean oil. A 0.1-mm-diameter nylon thread was used to suspend the synthetic tumor in the oil.

The skin layer in the phantom was created using a 1.5-mm-thick unclad FR4 glass epoxy PC board. According to the manufacturer, the dielectric properties of FR4 at 1 GHz are $\varepsilon_r = 4.34$, with a loss tangent of 0.016. Thus, the dielectric constant of the skin simulant fell in between that of the normal and malignant-tissue simulants, as desired.

During data collection, the UWB antenna was sequentially scanned in 1-cm increments to 49 different positions in a 6-cm × 6-cm array. The antenna element was positioned so that its aperture was 1 cm above the skin surface. The antenna was connected to an Agilent E8364A (10 MHz-50 GHz) performance network analyzer (PNA) to transmit and receive microwave signals. At each antenna location in the synthetic array, the network analyzer performed a frequency sweep from 1 to 11 GHz, with 201 frequency samples, and recorded the backscatter (S_{11} parameter). The frequency-domain backscattered signals were scaled by the spectrum of the desired input pulse, and transformed to the time domain using an inverse-FFT algorithm.

After measuring backscattered signals (S_{11}) from the multilayer breast phantoms, time-domain backscattered waveforms were synthesized. Next, as discussed in previous sections, dominant early-time artifacts were removed from the waveforms before three-dimensional MIST beamforming was employed to create an image of backscattered energy as a function of position.

Figure 12 shows the MIST beamforming results for the experimental breast phantom consisting of a 4-mm-diameter synthetic tumor placed 2 cm below the skin surface under the center of the array. The three-dimensional image of backscattered energy was generated for a 6-cm × 6-cm × 5-cm domain with a 1-mm pixel resolution. Three orthogonal planes from the three-dimensional image were labeled using x and y axes that corresponded to the lateral dimensions of the imaging domain, and a z axis that corresponded to the depth dimension. The origin of the z axis roughly corresponded to the location of the skin layer. The two energy peaks in the depth direction corresponded to scattering from the top and bottom surfaces of the compact cylindrical tumor. The peak energy nearest the surface was located within 2 mm of the top edge of the actual tumor. For comparison purposes, the same beamforming process was also applied to the backscattered waveforms obtained from a tumor-free phantom. The signal-to-clutter ratio (S/C), defined as the ratio of the maximum tumor energy to the maximum clutter energy in the tumor-free phantom, was 8.4 dB for this reduced-contrast scenario. Figure 12d plots the −3 dB contour of the MIST image, and illustrates the location of the energy peak generated by the tumor in three dimensions.

Figure 13 shows the −3 dB contour plots of the MIST beamforming results for the experimental breast phantom containing two 4-mm-diameter synthetic tumors separated by approximately 2 cm in the lateral direction. It is evident that the two tumors were accurately located and resolved in three dimensions.

6. Summary

In this article, we reviewed a UWB microwave-imaging technique that employs space-time beamforming for detecting small malignant breast tumors. Numerical studies based on two-dimensional FDTD simulations demonstrated the efficacy of the MIST beamforming method for detecting very small malignant lesions in heterogeneous breast tissue, in both the prone and supine configurations. The experimental feasibility of the MIST beamforming approach was also demonstrated in three dimensions, using an initial imaging prototype and a multilayered breast phantom containing one or more small synthetic tumors. The promising nature of the results from this body of work provides compelling rationale for further research to develop this low-power UWB microwave radar-imaging technique into a clinical diagnostic tool.

7. Acknowledgement

This work was supported by the Department of Defense Breast Cancer Research Program under award DAMD17-02-1-0625, the National Science Foundation under grant BES 0201880, the National Institutes of Health under grant R21 CA92188-01 awarded by the National Cancer Institute, and the National Institutes of Health under grant 1 F31 CA099933-01.

8. References

1. D. J. Daniels, *Surface-Penetrating Radar*, London, IEE Press, 1996.

2. S. C. Hagness, A. Taflove, and J. E. Bridges, "Two-Dimensional FDTD Analysis of a Pulsed Microwave Confocal System for Breast Cancer Detection: Fixed-Focus and Antenna-Array Sensors," *IEEE Transactions on Biomedical Engineering*, **45**, 12, December 1998, pp. 1470-1479.

3. S. C. Hagness, A. Taflove, and J. E. Bridges, "Three-Dimensional FDTD Analysis of a Pulsed Microwave Confocal System for Breast Cancer Detection: Design of an Antenna-Array Element," *IEEE Transactions on Antennas and Propagation*, **AP-47**, 5, May 1999, pp. 783-791.

4. R. Sedledskii, "Application of Sub-Surface Radar in Detecting Affected Mammary Gland Tissues," *J. Communications Technology and Electronics*, **45**, 9, September 2000, pp. 1009-1016.

5. X. Li and S. C. Hagness, "A Confocal Microwave Imaging Algorithm for Breast Cancer Detection," *IEEE Microwave and Wireless Components Letters*, **11**, 3, March 2001, pp. 130-132.

6. E. J. Bond, X. Li, S. C. Hagness, and B. D. Van Veen, "Microwave Imaging via Space-Time Beamforming for Early Detection of Breast Cancer," *IEEE Transactions on Antennas and Propagation*, **AP-51**, 8, August 2003, pp. 1690-1705.

7. S. K. Davis, E. J. Bond, X. Li, S. C. Hagness, and B. D. Van Veen, "Microwave Imaging via Space-Time Beamforming for Early Detection of Breast Cancer: Beamformer Design in the Frequency Domain," *Journal of Electromagnetic Waves and Applications*, **17**, 2, 2003, pp. 357-381.

8. X. Li, S. K. Davis, S. C. Hagness, D. W. van der Weide, and B. D. Van Veen, "Microwave Imaging via Space-Time Beamforming: Experimental Investigation of Tumor Detection in Multi-Layer Breast Phantoms," *IEEE Transactions on Microwave Theory and Techniques*, **MTT-52**, 8, August 2004, pp. 1856-1865.

9. E. C. Fear and M. A. Stuchly, "Microwave Detection of Breast Cancer," *IEEE Transactions on Microwave Theory and Techniques*, **MTT-48**, 11, November 2000, pp. 1854-1863.

10. E. C. Fear, J. Sill, and M. A. Stuchly, "Experimental Feasibility Study of Confocal Microwave Imaging for Breast Tumor Detection," *IEEE Transactions on Microwave Theory and Techniques*, **MTT-51**, March 2003, pp. 887-892.

11. R. Nilavalan, A. Gbedemah, I. J. Craddock, X. Li, and S. C. Hagness, "Numerical Investigation of Breast Tumor Detection Using Multi-Static Radar," *Electronics Letters*, **39**, 25, 2003, pp. 1787-1788.

12. M. A. Hernandez-Lopez, M. Quintillan-Gonzalez, S. G. Garcia, A. R. Bretones, and R. G. Martin, "A Rotating Array of Antennas for Confocal Microwave Breast Imaging," *Microwave and Optical Technology Letters*, **39**, 4, 2003, pp. 307-311.

13. M. El-Shenawee, "Resonant Spectra of Malignant Breast Cancer Tumors Using the Three-Dimensional Electromagnetic Fast Multipole Model," *IEEE Transactions on Biomedical Engineering*, **51**, 1, 2004, pp. 35-44.

14. Y. Huo, R. Bansal, and Q. Zhu, "Modeling of Noninvasive Microwave Characterization of Breast Tumors," *IEEE Transactions on Biomedical Engineering*, **51**, 7, July 2004, pp. 1089-1094.

15. *Mammography and Beyond: Developing Techniques for the Early Detection of Breast Cancer*, Washington, DC, Institute of Medicine, National Academy Press, 2000.

16. P. T. Huynh, A. M. Jarolimek, and S. Daye, "The False-Negative Mammogram," *Radiographics*, **18**, 5, 1998, pp. 1137- 1154.

17. J. G. Elmore, M. B. Barton, V. M. Moceri, S. Polk, P. J. Arena, and S. W. Fletcher, "Ten-Year Risk of False Positive Screening Mammograms and Clinical Breast Examinations," *New Engl. J. Med.*, **338**, 16, 1998, pp. 1089-1096.

18. S. S. Chaudhary, R. K. Mishra, A. Swarup, and J. M. Thomas, "Dielectric Properties of Normal and Malignant Human Breast Tissues at Radiowave and Microwave Frequencies," *Indian J. Biochem. and Biophys.*, **21**, February 1984, pp. 76-79.

19. A. J. Surowiec, S. S. Stuchly, J. R. Barr, and A. Swarup, "Dielectric Properties of Breast Carcinoma and the Surrounding Tissues," *IEEE Transactions on Biomedical Engineering*, **35**, April 1988, pp. 257-263.

20. W. T. Joines, Y. Z. Dhenxing, and R. L. Jirtle, "The Measured Electrical Properties of Normal and Malignant Human Tissues from 50 to 900 MHz," *Med. Phys.*, **21**, April 1994, pp. 547-550.

21. K. R. Foster and H. P. Schwan, "Dielectric Properties of Tissues and Biological Materials: A Critical Review," *Critical Reviews for Biomedical Engineering*, **17**, 1989, pp. 25-104.

22. A. S. Swarup, S. S. Stuchly, and A. Surowiec, "Dielectric Properties of Mouse MCA1 Fibrosarcoma at Different Stages of Development," *Bioelectromagnetics*, **12**, 1991, pp. 1-8.

23. K. S. Osterman, T. E. Kerner, D. B. Williams, A. Hartov, S. P. Poplack, and K. D. Paulsen, "Multifrequency Electrical Impedance Imaging: Preliminary in vivo Imaging in the Breast," *Physiol. Meas.*, **21**, 2000, pp. 99-109.

24. J. Mueller, S. Siltanen, and D. Isaacson, "A Direct Reconstruction Algorithm for Electrical Impedance Tomography," *IEEE Trans. Med. Imag.*, **21**, 6, 2002, pp. 555-559.

25. T. O. McBride, B. W. Pogue, S. Jiang, U. L. Osterberg, K. D. Paulsen, and S. P. Poplack, "Initial Studies of in vivo Absorbing and Scattering Heterogeneity in Near-Infrared Tomographic Breast Imaging," *Optics Letters*, **26**, 2001, pp. 822-824.

26. P. M. Meaney, M. W. Fanning, D. Li, S. P. Poplack, and K. D. Paulsen, "A Clinical Prototype for Active Microwave Imaging of the Breast," *IEEE Transactions on Microwave Theory and Techniques*, **MTT-48**, 11, November 2000, pp. 1841-1853.

27. A. E. Bulyshev, S. Y. Semenov, A. E. Souvorov, R. H. Svenson, A. G. Nazarov, Y. E. Sizov, and G. P. Tatsis, "Computational Modeling of Three-Dimensional Microwave Tomography of Breast Cancer," *IEEE Transactions on Biomedical Engineering*, **48**, 9, September 2001, pp. 1053-1056.

28. Z. Q. Zhang, Q. Liu, C. Xiao, E. Ward, G. Ybarra, and W. T. Joines, "Microwave Breast Imaging: 3-D Forward Scattering Simulation," *IEEE Transactions on Biomedical Engineering*, **50**, 10, October 2003, pp. 1180-1189.

29. E. Fear, X. Li, S. C. Hagness, and M. A. Stuchly, "Confocal Microwave Imaging for Breast Cancer Detection: Localization of Tumors in Three Dimensions," *IEEE Transactions on Biomedical Engineering*, **49**, August 2002, pp. 812-822.

30. H. L. Van Trees, *Optimum Array Processing*, New York, Wiley-Interscience, 2002.

31. W. H. Parsons, *Cancer of the Breast*, Springfield, IL, Charles Thomas, 1959.

32. S. Haykin, *Adaptive Filter Theory, Third Edition*, New Jersey, Prentice-Hall, 1996.

33. B. Van Veen and K. Buckley, "Beamforming: A Versatile Approach to Spatial Filtering," *IEEE ASSP Magazine*, **5**, April 1988, pp. 4-24.

34. S. K. Davis, X. Li, E. J. Bond, S. C. Hagness, and B. D. Van Veen, "Frequency-Domain Penalized Least-Squares Beamformer Design for Early Detection of Breast Cancer via Microwave Imaging," in *IEEE Sensor Array and Multichannel Signal Processing Workshop*, Rosslyn, VA, August 2002, pp. 120-124.

35. A. Taflove and S. Hagness, *Computational Electrodynamics: The Finite-Difference Time-Domain Method, Second Edition*, Norwood, MA, Artech House, 2000.

36. X. Li, S. C. Hagness, M. K. Choi, and D. W. van der Weide, "Numerical and Experimental Investigation of an Ultrawideband

Ridged Pyramidal Horn Antenna with Curved Launching Plane for Pulse Radiation," *IEEE Antennas and Wireless Propagation Letters*, **2**, 2003, pp. 259-262.

37. S. S. Stuchly, C. L. Sibbald, and J. M. Anderson, "A New Aperture Admittance Model for Open-Ended Waveguides," *IEEE Transactions on Microwave Theory and Techniques*, **MTT-42**, 2, February 1994, pp. 192-198.

Introducing the Feature Article Authors

Xu Li received the BS degree in Biomedical Engineering from Tsinghua University, Beijing, China in 1998. She received the MS degree in Biomedical Engineering in 2000 and the PhD degree in Electrical and Computer Engineering in 2003, both from the University of Wisconsin-Madison. Since October of 2003, she has been working as a postdoctoral fellow and, subsequently, as a research associate in the Department of Biomedical Engineering, Northwestern University. Her research interests include applied and computational electromagnetics, bioelectromagnetics, biophotonics, and optical devices for nano-biotechnology.

Essex Bond was born in Milwaukee, Wisconsin. He received the BS degree from the Milwaukee School of Engineering in 1999, and the MS degree from the University of Wisconsin-Madison in August, 2001, both in Electrical Engineering. He is currently pursuing his PhD degree in the Department of Electrical and Computer Engineering at the University of Wisconsin-Madison. He is the recipient of a National Institutes of Health Pre-doctoral Fellowship. His research interests include array signal processing, biomedical applications of signal processing, and microwave imaging techniques.

Barry D. Van Veen was born in Green Bay, Wisconsin. He received the BS degree from Michigan Technological University in 1983, and the PhD degree from the University of Colorado in 1986, both in Electrical Engineering. He was an ONR Fellow while working on the PhD degree.

In the spring of 1987, he was with the Department of Electrical and Computer Engineering at the University of Colorado-Boulder. Since August of 1987, he has been with the Department of Electrical and Computer Engineering at the University of Wisconsin-Madison, and currently holds the rank of Professor. His research interests include signal processing for sensor arrays, wireless communications, and biomedical applications of signal processing.

Dr. Van Veen was a recipient of a 1989 Presidential Young Investigator Award from the National Science Foundation, and a 1990 IEEE Signal Processing Society Paper Award. He served as an Associate Editor for the *IEEE Transactions on Signal Processing* and on the IEEE Signal Processing Society's Statistical Signal and Array Processing Technical Committee and the Sensor Array and Multichannel Technical Committee. He is a Fellow of the IEEE, and received the Holdridge Teaching Excellence Award from the ECE Department at the University of Wisconsin in 1997. He coauthored "Signals and Systems," (first edition, 1999; second edition, 2003; Wiley) with Simon Haykin.

Susan C. Hagness received the BS (with highest honors) and PhD degrees in Electrical Engineering from Northwestern University, Evanston, IL, in 1993 and 1998, respectively. While working toward the PhD degree, she was a National Science Foundation (NSF) Graduate Fellow and a Tau Beta Pi Spencer Fellow.

Since August, 1998, she has been with the University of Wisconsin-Madison, where she is currently an Associate Professor with the Department of Electrical and Computer Engineering, and a faculty affiliate with the Department of Biomedical Engineering. Her research interests include FDTD theory and applications in photonics and bioelectromagnetics, as well as microwave imaging, sensing, and thermal therapy techniques in biological and medical applications. She coauthored *Computational Electrodynamics: The Finite-Difference Time-Domain Method* (second edition, 2000, Artech House).

Xu Li

Essex Bond

Barry D. Van Veen

Susan C. Hagness